01 Nov 2017

An Embeddable Optical Strain Gauge based on a Buckled Beam

Yang Du

Yizheng Chen

Chen Zhu

Yiyang Zhuang

et. al. For a complete list of authors, see https://scholarsmine.mst.edu/ele_comeng_facwork/3260

Recommended Citation

Y. Du et al., "An Embeddable Optical Strain Gauge based on a Buckled Beam," *Review of Scientific Instruments*, vol. 88, no. 11, American Institute of Physics (AIP), Nov 2017.
The definitive version is available at https://doi.org/10.1063/1.5004109

An embeddable optical strain gauge based on a buckled beam

Yang Du,[a] Yizheng Chen,[a] Chen Zhu, Yiyang Zhuang, and Jie Huang[b]
Department of Electrical and Computer Engineering, Missouri University of Science and Technology, Rolla, Missouri 65409, USA

(Received 11 September 2017; accepted 12 October 2017; published online 1 November 2017)

We report, for the first time, a low cost, compact, and novel mechanically designed extrinsic Fabry-Perot interferometer (EFPI)-based optical fiber sensor with a strain amplification mechanism for strain measurement. The fundamental design principle includes a buckled beam with a coated gold layer, mounted on two grips. A Fabry-Perot cavity is produced between the buckled beam and the endface of a single mode fiber (SMF). A ceramic ferrule is applied for supporting and orienting the SMF. The principal sensor elements are packaged and protected by two designed metal shells. The midpoint of the buckled beam will experience a deflection vertically when the beam is subjected to a horizontally/axially compressive displacement. It has been found that the vertical deflection of the beam at midpoint can be 6–17 times larger than the horizontal/axial displacement, which forms the basis of a strain amplification mechanism. The user-configurable buckling beam geometry-based strain amplification mechanism enables the strain sensor to achieve a wide range of strain measurement sensitivities. The designed EFPI was used to monitor shrinkage of a square brick of mortar. The strain was measured during the drying/curing stage. We envision that it could be a good strain sensor to be embedded in civil materials/structures under a harsh environment for a prolonged period of time. *Published by AIP Publishing.* https://doi.org/10.1063/1.5004109

I. INTRODUCTION

Strain measurements based on optical fiber sensors have been widely studied over the past few decades. They have been applied in many engineering areas including civil, power, and aerospace due to their well-known merits such as compact size, light weight, high sensitivity, immunity to electromagnetic interference, and the ability for long distance measurements.[1] Various types of optical fiber strain sensors have been studied, such as fiber Bragg grating (FBG) sensors,[2] long-period fiber grating (LPFG) strain sensors,[3] multimode interference-based polymer optical fiber strain sensors,[4] fiber-in-line Mach-Zehnder interferometric strain sensors,[5] intrinsic or extrinsic Fabry-Perot (FP) fiber-optic sensors,[6,7] Brillouin or Rayleigh scattering distributed strain sensors.[8,9]

Concerning the applications in the real world, most of the aforementioned optical fiber strain sensors have to encounter the challenges of costly economic investment, fragile structures, complex configurations, or complicated signal processing. For instance, FBG and LPFG sensors are presented with a large sensing range and high sensitivity for strain measurements.[2,3] However, the production of them is costly and complicated. The fabrication processes always involve a phase mask, a UV laser, or a CO_2 laser. Moreover, material fatigue is an important issue for the FBG sensors and LPFG sensors in applications with a prolonged time.[10] And a multimode interference-based polymer optical fiber strain sensor always has a limited strain measurement resolution.[4] In the case of fiber-in-line Mach-Zehnder interferometric strain sensors, their mechanical strength always limits the stability of the sensing applications due to the fiber tapering or chemical etching processes.[5,11] As the thermal expansion coefficient is small in the air cavities produced in the fiber, intrinsic FP fiber-optic sensors have been proposed for pressure and strain measurements.[12–14] Unfortunately, complicated pretreatments are always needed for the fabrication of an FP cavity in the fiber. For example, the fabrication of intrinsic FP cavities, which are usually manufactured with a femtosecond laser, requires a stringent alignment and positioning system.[13] Additionally, air cavity-based FP sensors are usually proposed by assembling special optical fiber structures. For instance, solid-core photonic crystal fibers,[15] hollow-core photonic crystal fibers,[6,16] or silica capillaries,[17,18] which may induce long-term signal drifts especially in a high-temperature environment due to the assembly method. Both BOTDR (Brillouin optical time domain reflectometry) and OFDR (optical frequency domain reflectometry) methods can realize distributed strain sensing with spatial resolution on the scale of centimeters.[8,9] However, due to the inherently low scattering rates, both of these techniques require equipment with much higher cost than the interrogators for the aforementioned point-sensors and complicated signal processing. Also, in practical applications, kilometers-long distributed optical fiber strain sensors embedded in a civil structure potentially possess a high risk of damaging the entire sensors concurrently.

In comparison to the aforementioned sensors, the extrinsic Fabry-Perot interferometer (EFPI) has the advantage for strain measurements. An EFPI cavity is typically constructed by two endfaces of the optical fibers or two mirrors in free space. The reflective spectrum from an EFPI is determined by the length between the two reflecting surfaces.[19,20] Furthermore, the air cavity-based EFPI can be flexibly designed to compensate the temperature influence.[20] Many reported EFPI sensors are used for displacement measurements.[20–22]

[a]Y. Du and Y. Chen contributed equally to this work.
[b]Author to whom correspondence should be addressed: jieh@mst.edu

A strain sensor can be implemented by translating the absolute displacement of the cavity length into strain. Therefore, EFPI sensors could be considered as good candidates for strain measurements with proper structure design and packaging.[20,23] Most commonly reported EFPI strain sensors are designed as fiber-in-capillary type sensors.[23,24] These types of sensors have to encounter some challenges during practical applications. First, the fiber-in-capillary package EFPI is difficult to fabricate because of the complicated alignment processes. Second, the fiber-in-capillary package design was found to have a long-term drift especially in a high-temperature environment due to the assembly method.[25] Third, the elongation of an EFPI induced by strain is insufficient to provide a promising strain sensitivity for many practical applications. In order to overcome the deleterious issues of the traditional EFPI strain sensors, a smart mechanical design of an EFPI sensor including a compact packaging process with high mechanical strength and a strain amplification mechanism is highly desired.

In this paper, we report and present a novel and compact mechanically designed EFPI strain sensor. For the first time to our knowledge, a buckled beam geometry-based strain amplification mechanism is employed. This proposed novel mechanical design is user-configurable. For example, the buckled beam-based mechanical design can increase the axial displacement by 6–17 times. Our designed sensor consists of a buckled beam with a gold-coated layer mounted on two grips. An FP cavity is then formed by the gold-coated layer of the buckled beam and the endface of a single mode fiber (SMF). The principal sensor elements are packaged and protected using two metal shells. The vertical deflection at the midpoint of the buckled beam will be amplified when the beam is subjected to a horizontally/axially compressive strain. As the sensor experiences an axial strain, it will be translated to a vertical displacement at the midpoint of the buckled beam captured by an EFPI sensor. In our calibration experiment, a displacement amplification factor of 6.5 is achieved. The designed sensor was also applied to monitoring the shrinkage strain of mortar in two weeks, demonstrating the practicability of the sensor.

II. SENSOR DESIGN AND MEASUREMENT PRINCIPLE

A schematic drawing of the strain sensor is illustrated in Fig. 1, including an optical fiber component and a buckled beam with a rectangular cross section. The beam is pinned by two grips at both ends. The surface of the beam close to the endface of the fiber is coated with a thin layer of gold, with a reflectivity of 99%, to serve as a mirror. The endface of the SMF is parallel to the coated layer. Therefore, an air cavity is realized between the endface of the SMF and its corresponding mirror.

When the column beam is subjected to an axially compressive stress, buckling occurs. This leads to bending or deflection of the beam due to the elasticity of the beam.[26] It should be noted that the analysis for the buckled beam model is based on the following assumptions:

(1) The beam is initially straight.
(2) The load applied to the beam is axial, with no eccentricity.

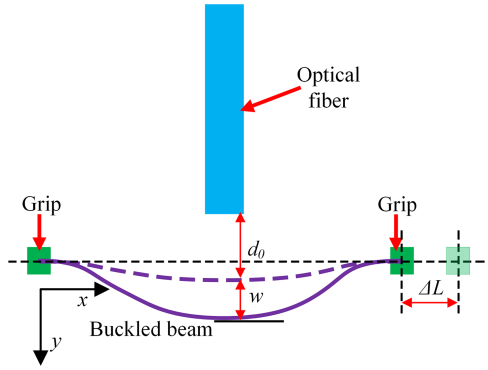

FIG. 1. A schematic drawing of a EFPI sensor for strain sensing. The sensor consists of the optical fiber and a long-column beam. The beam is pinned by two grips at both ends. One surface of the beam is coated with a thin gold layer, with a reflectivity of 99%, to serve as a mirror.

(3) The beam is pinned at both ends.

According to the classical Euler buckling theory,[26] the critical (or Euler) buckling load Pcr can be calculated by the following formula:[26]

$$P_{cr} = \frac{4\pi^2 EI}{(L-\Delta L)^2}, \tag{1}$$

where E is the modulus of elasticity, I is the moment of inertia of the beam, $I = bh^3/12$, where b is the width of the beam and h is the thickness of the beam, and L is the length of the beam. According to the Euler buckling theory,[26] the shape function for the buckled shape $y(x)$ is mathematically given by[26]

$$y = -\frac{M_0}{P_{cr}}\cos\left(\sqrt{\frac{P_{cr}}{EI}}x\right) + \frac{M_0}{P_{cr}}, \tag{2}$$

where M_0 is the initial bending moment and x is the axial displacement of the buckled beam. Substituting Eq. (1) into Eq. (2), we can obtain the relationship between the deflection at the midpoint of the buckled beam w and the line segment length along the column beam ΔL, which is given by

$$w = \frac{M_0(L-\Delta L)^2}{2EI\pi^2}. \tag{3}$$

A traditional solution to the nonlinear, large-deflection beam equations is solved by elliptic integral.[27] In other words, we can transform the mechanical model into a geometry equation. The deflection at the midpoint of the buckled beam can be solved by the incomplete elliptic integrals of the second kind,[28] which can be expressed as

$$L = w\int_0^{\pi}\sqrt{1-k^2\sin^2\theta}\,d\theta, \tag{4}$$

where $K^2 = 1 - [(L - \Delta L)/2w]^2$, ΔL is defined as the line segment length along the curve of the beam (axial displacement of the buckled beam), $d\theta$ is the infinitesimal width, and θ ranges from 0 to π. From Eq. (4), we can find out that the deflection at the midpoint of the buckled column w is only related to the length of the beam L and axial displacement of the buckled beam ΔL. A plot of this function, treating ΔL as a continuous variable and setting the length of the beam L as 24 mm, is given in Fig. 2(a). The derivative of the deflection

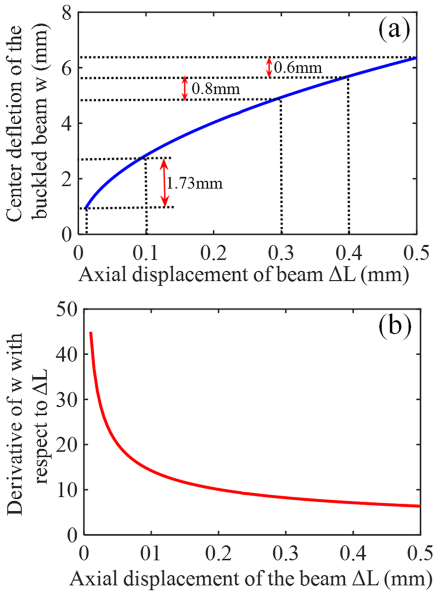

FIG. 2. (a) The relationship between the center deflection of the buckled beam w and the axial displacement along the beam ΔL. (b) The derivative of the center deflection of the buckled beam w with respect to the axial displacement along the beam ΔL.

at the midpoint of the buckled beam w with respect to ΔL is plotted in Fig. 2(b). From Fig. 2(a), we learnt that the variation of the deflection at the midpoint of the buckled beam is much larger than the axial displacement. In other words, the axial displacement can be translated to the vertical displacement at the midpoint of the buckled beam with an amplification factor. For instance, when the axial displacement of the buckled beam is from 0 to 0.1 mm, the center deflection of the buckled beam is 1.73 mm, which is about 17 times larger than the axial displacement; when the axial displacement of the buckled beam is from 0.3 to 0.4 mm, the center deflection of the buckled beam is 0.8 mm, which is about 8 times larger than the axial displacement. Figure 2(b) represents the amplification factors at various compressive displacements/strains. The amplification factor decreases as the strain increases. Considering the length of a typical EFPI cavity, this amplification factor can increase the axial displacement by 6–17 times.

As presented earlier, the cavity length d ($d = d_0 + w$, where d_0 is the initial distance between the optical fiber and the pre-buckled beam, as shown in Fig. 1) is formed between the endface of the SMF and the coated gold layer on the surface of the buckled beam. The demodulation principle is similar to our previous work.[7,20] The physical length of the FP cavity can be determined by the free spectrum range (FSR) of the recorded interference spectrum. The pre-buckled beam will experience a deflection at its midpoint when the beam is subjected to axially compressive stress, resulting in a change Δd of the cavity length which can be determined by

$$\Delta d = \frac{\lambda^2 \Delta FSR}{FSR_1 FSR_2}. \quad (5)$$

where FSR_1 and FSR_2 are the values of FSR before and after a deflection and λ is the free-space wavelength. Therefore, the deflection at the midpoint of the buckled beam can be obtained. Accordingly, the displacement ΔL from the measurement grip could be further determined. Finally, the strain ε applied on the beam can be calculated by $\varepsilon = \Delta L/L$. Importantly, the actual axial displacement of the beam is transferred and amplified to the vertical deflection at the center of the buckled beam. The measured strain sensitivity is adjustable according to the initial deflection at the center of the beam as shown in Fig. 2(a).

III. EXPERIMENTAL RESULTS AND DISCUSSIONS

The mechanical design of the buckled beam-based strain sensor is shown in Fig. 3(a). The designed sensor consists of two metal shells. The two metal shells can be assembled by inserting the right one into the left one. A sealed component and two grips are incorporated into the two metal shells. As a result, a sealed cavity is formed inside the metal shells. A buckled beam (length × width × height: 24 mm × 3 mm × 0.2 mm) with a coated gold layer is pinned by two grips at both ends. An SMF is packaged in a ceramic ferrule and immobilized in the left metal shell through a drilled hole on top. The lead-out SMF with a fiber-optic protection sleeve is then sealed by a sealing ring. Therefore, an EFPI is formed by the SMF endface and its corresponding mirror at the center beam. When the limit discs on both metal shells are subjected to axially compressive stress, the inner pre-buckled beam will experience a deflection and result in a change in EFPI cavity length. The principle sensor elements are packaged in two metal shells. These two

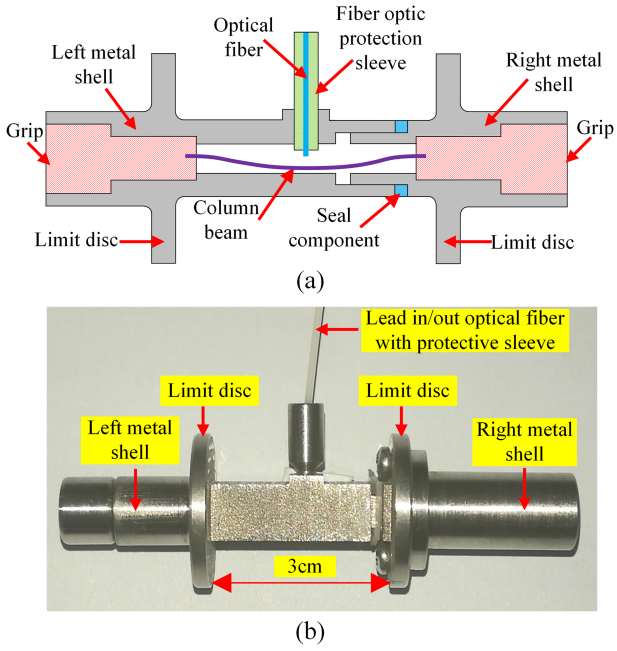

FIG. 3. (a) Mechanical design of the buckled beam-based strain sensor. The two metal shells can be assembled by inserting the right one into the left one. A sealed component and two grips are incorporated into the two metal shells. As a result, a sealed cavity is formed inside the metal shells. A buckled beam (length × width × height: 24 mm × 3 mm × 0.2 mm) with a coated gold layer is pinned by two grips at both ends. An SMF is packaged in a fiber ceramic ferrule and immobilized inside the left metal shell through a drilled hole on top. The output SMF is fixed with a fiber-optic protection sleeve by a sealing ring. The mirror and the endface of the corresponding SMF are parallel, such that an EFPI is formed. (b) A photograph of our sensor. The sensor is packaged with two metal shells. The initial distance between the limit discs on both metal shells is 3 cm.

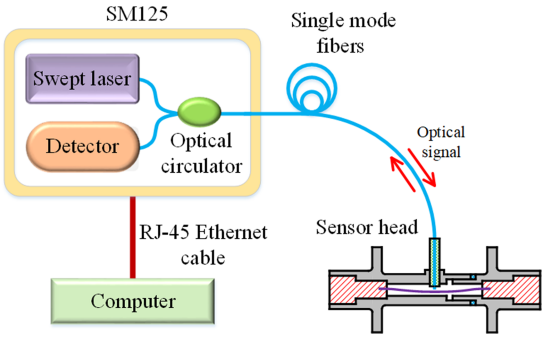

FIG. 4. Schematic diagram of the experimental setup. The input-output optical fiber is connected to the EFPI-based strain sensor.

metal shells ensure a dust-free environment. A photograph of our fabricated optical fiber strain sensor is shown in Fig. 3(b). The initial distance between the limit discs on both metal shells is 3 cm. Our designed EFPI-based strain sensor can achieve a high sensing sensitivity due to the strain amplification mechanism, up to 17 times larger. The prototype sensor is designed to be embedded in civil structures/materials for long-term real time strain monitoring.

The experimental setup for the EFPI-based strain sensor is illustrated in Fig. 4. An integrated optical interrogator from Micron Optics is used as the demodulation device, and a lead-in SMF from the interrogator is directly connected to the proposed sensor. A computer is used for signal interrogation and processing. The detailed description of the system setup and signal processing can be found in our previous studies.[7,20]

Prior to demonstrating the sensor in practical applications, we first calibrated the sensor. In the calibration experiment, we used a micrometer (Mitutoyo) (displacement resolution: 0.1 μm, dynamic range: 25 mm) to apply compressive strain on both limit discs. The relationship between the applied axial displacement and the cavity length variation of our strain sensor is shown in Fig. 5. The displacement between the two limit

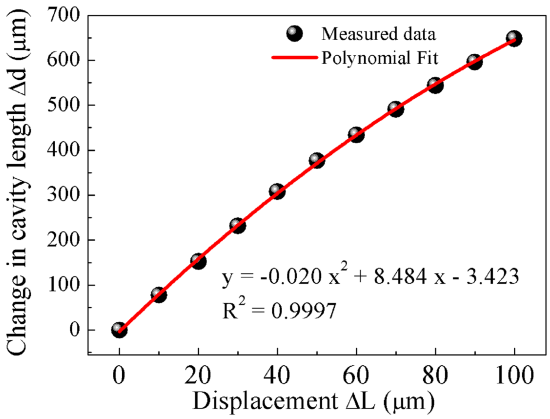

FIG. 5. The relationship between the applied axial displacement and the change in the cavity length of the EFPI sensor. The displacement between the two limit discs ranges from 0 to 100 μm with the step of 10 μm. A polynomial fit was applied to the measured data. The relationship between the cavity length variation of the EFPI and the displacement between the two limit discs can be expressed as $y = -0.02x^2 + 8.484x - 3.423$, where y and x are the same as Δd and ΔL, respectively. The R-square of the fitting is up to 0.9997.

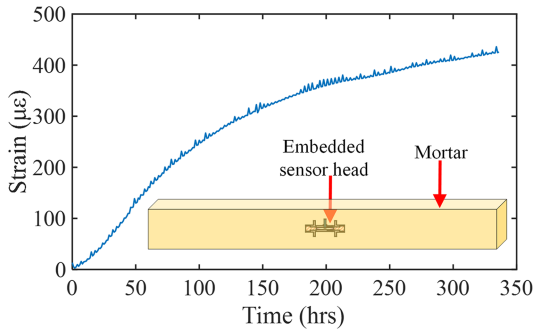

FIG. 6. Real-time shrinkage strain measurement. The inset is the illustration of the experimental setup for shrinkage monitoring. The strain sensor was initially embedded in the mortar during the casting process. Mortar composition and weight ratios: Sakrete Portland Type-1 cement, 1.0; tap water, 0.5; sand, 2.8. Brick of mortar size: 254 × 25.4 × 25.4 mm.

discs ranges from 0 to 100 μm with the step of 10 μm. A polynomial fit was applied to the measured data. The relationship between the variation in the cavity length of the EFPI and the displacement between the two limit discs can be expressed as $y = -0.02x^2 + 8.484x - 3.423$, where y and x are the same as Δd and ΔL, respectively. The R-square of the fitting is up to 0.9997. Accordingly, based on the calibrated fitting curve, an externally applied displacement on the sensor can be resolved by the measured variation in the cavity length of the EFPI. So the corresponding strain ε applied on the sensor can be further calculated by $\Delta L/L$ (where L equals 3 cm). The amplification factor of the fabricated sensor was demonstrated to be 6.5 times.

We performed a lab test to monitor the shrinkage process of a brick of mortar during its drying/curing stage for two weeks to demonstrate its practical use in real-world applications. The detailed information regarding the preparation of the mortar is described in Ref. 20. Our strain sensor was initially embedded in the mortar during the casting process. The mortar was located in a temperature-controlled box. The axial strain was applied to the embedded sensor due to the shrinkage of mortar. The schematic diagram of the experimental setup is illustrated as an inset in Fig. 6.

The measurement results for monitoring shrinkage strain of mortar are shown in Fig. 6. The shrinkage strain monitoring experiment lasted for two weeks. It can be observed that the shrinkage strain along the long axis of the brick of mortar increased with time. The results of strain matched well with the reported literature.[29] The small ripples in the curve were caused by the temperature variations in the temperature-controlled box due to the regulation of refrigeration. From Fig. 6, we can conclude that our designed strain sensor can work continuously for a long time, which is a key for real-world applications. It should be noted that an FBG sensor can be integrated to the fiber end section for temperature compensation.

IV. CONCLUSION

In conclusion, we invented and demonstrated a simple and compact EFPI-based fiber-optic sensor for strain measurements using a buckled beam. A user-configurable buckling

beam-based strain amplification mechanism was employed, enabling a wide range of strain sensitivities. Theoretically, this amplification factor can increase the axial displacement by 6–17 times. Our designed sensor consists of a buckled beam with a gold-coated layer mounted on two grips. So an FP cavity is produced between the buckled beam and the endface of an SMF. The principal sensor is packaged and protected by two designed metal shells. In our calibration experiment, a displacement amplification factor of 6.5 was achieved. The fabricated sensor was employed to monitor the shrinkage of a brick of mortar for two weeks. The proposed sensor prototype is compact, robust, and easy to manufacture/commercialize. We envision that a good strain sensor could be embedded in reinforcing bars and concrete and other civil materials/structures under a harsh environment for a prolonged period of time.

ACKNOWLEDGMENTS

This work was supported by the University of Missouri Research Board, the Materials Research Center at Missouri S&T, and the ISC Postdoctoral Matching Funds at Missouri S&T.

[1]Z. Chen, G. Hefferman, and T. Wei, "Terahertz-range weak reflection fiber optic structures for sensing applications," IEEE J. Sel. Top. Quantum Electron. **23**, 1–6 (2017).
[2]O. Xu, J. Zhang, H. Deng, and J. Yao, "Dual-frequency optoelectronic oscillator for thermal-insensitive interrogation of a FBG strain sensor," IEEE Photonics Technol. Lett. **29**, 357–360 (2017).
[3]Y. P. Wang, L. Xiao, D. N. Wang, and W. Jin, "Highly sensitive long-period fiber-grating strain sensor with low temperature sensitivity," Opt. Lett. **31**, 3414–3416 (2006).
[4]J. Huang, X. Lan, H. Wang, L. Yuan, T. Wei, Z. Gao, and H. Xiao, "Polymer optical fiber for large strain measurement based on multimode interference," Opt. Lett. **37**, 4308–4310 (2012).
[5]A. A. Jasim, N. Hayashi, S. W. Harun, H. Ahmad, R. Penny, Y. Mizuno, and K. Nakamura, "Refractive index and strain sensing using inline Mach–Zehnder interferometer comprising perfluorinated graded-index plastic optical fiber," Sens. Actuators, A **219**, 94–99 (2014).
[6]Y. Wu, Y. Zhang, J. Wu, and P. Yuan, "Temperature-insensitive fiber optic Fabry-Perot interferometer based on special air cavity for transverse load and strain measurements," Opt. Express **25**, 9443–9448 (2017).
[7]Y. Du, Y. Chen, Y. Zhuang, C. Zhu, F. Tang, and J. Huang, "Probing nanostrain via a mechanically designed optical fiber interferometer," IEEE Photonics Technol. Lett. **29**, 1348–1351 (2017).
[8]Y. Weng, E. Ip, Z. Pan, and T. Wang, "Single-end simultaneous temperature and strain sensing techniques based on Brillouin optical time domain reflectometry in few-mode fibers," Opt. Express **23**, 9024–9039 (2015).
[9]D. Wada, H. Igawa, and T. Kasai, "Vibration monitoring of a helicopter blade model using the optical fiber distributed strain sensing technique," Appl. Opt. **55**, 6953–6959 (2016).
[10]J. Chen, J. Zhou, and Z. Jia, "High-sensitivity displacement sensor based on a bent fiber Mach–Zehnder interferometer," IEEE Photonics Technol. Lett. **25**, 2354–2357 (2013).
[11]Z. Tian and S. S. H. Yam, "In-line abrupt taper optical fiber Mach–Zehnder interferometric strain sensor," IEEE Photonics Technol. Lett. **21**, 161–163 (2009).
[12]H. Bae and M. Yu, "Miniature Fabry-Perot pressure sensor created by using UV-molding process with an optical fiber based mold," Opt. Express **20**, 14573–14583 (2012).
[13]T. Wei, Y. Han, H. L. Tsai, and H. Xiao, "Miniaturized fiber inline Fabry-Perot interferometer fabricated with a femtosecond laser," Opt. Lett. **33**, 536–538 (2008).
[14]S. Pevec and D. Donlagic, "All-fiber, long-active-length Fabry-Perot strain sensor," Opt. Express **19**, 15641–15651 (2010).
[15]F. C. Favero, L. Araujo, G. Bouwmans, V. Finazzi, J. Villatoro, and V. Pruneri, "Spheroidal Fabry-Perot microcavities in optical fibers for high-sensitivity sensing," Opt. Express **20**, 7112–7118 (2012).
[16]M. S. Ferreira, J. Bierlich, J. Kobelke, K. Schuster, J. L. Santos, and O. Frazão, "Towards the control of highly sensitive Fabry-Pérot strain sensor based on hollow-core ring photonic crystal fiber," Opt. Express **20**, 21946–21952 (2012).
[17]Y. Wang, D. N. Wang, C. Wang, and T. Hu, "Compressible fiber optic micro-Fabry-Pérot cavity with ultra-high pressure sensitivity," Opt. Express **21**, 14084–14089 (2013).
[18]A. Kaur, S. E. Watkins, J. Huang, L. Yuan, and H. Xiao, "Microcavity strain sensor for high temperature applications," Opt. Eng. **53**, 017105 (2014).
[19]B. H. Lee, Y. H. Kim, K. S. Park, J. B. Eom, M. J. Kim, B. S. Rho, and H. Y. Choi, "Interferometric fiber optic sensors," Sensors **12**, 2467–2486 (2012).
[20]C. Zhu, Y. Chen, Y. Du, Y. Zhuang, F. Liu, R. Gerald, and J. Huang, "A displacement sensor with centimeter dynamic range and submicrometer resolution based on an optical interferometer," IEEE Sens. J. **17**, 5523–5528 (2017).
[21]X. Zhou and Q. Yu, "Wide-range displacement sensor based on fiber-optic Fabry–Perot interferometer for subnanometer measurement," IEEE Sens. J. **11**, 1602–1606 (2011).
[22]Y. Bai, F. Yan, S. Liu, and X. Wen, "All fiber Fabry–Pérot interferometer for high-sensitive micro-displacement sensing," Opt. Quantum Electron. **48**, 206 (2016).
[23]J. A. Etches and G. F. Fernando, "Evaluation of embedded optical fiber sensors in composites: EFPI sensor response to fatigue loading," Polym. Compos. **31**, 284–291 (2010).
[24]J. Zhang, G. D. Peng, L. Yuan, and W. Sun, "Composite-cavity-based Fabry-Perot interferometric strain sensors," Opt. Lett. **32**, 1833–1835 (2007).
[25]P. Chawah, A. Sourice, G. Plantier, H. C. Seat, F. Boudin, J. Chery, M. Cattoen, P. Bernard, C. Brunet, S. Gaffet, and D. Boyer, "Amplitude and phase drift correction of EFPI sensor systems using both adaptive Kalman filter and temperature compensation for nanometric displacement estimation," J. Lightwave Technol. **30**, 2195–2202 (2012).
[26]H. E. Lindberg and A. L. Florence, *Dynamic Pulse Buckling: Theory and Experiment* (Martinus Nijhoff, Dordrecht, 1987), pp. 2–73.
[27]A. Midha, S. G. Bapat, A. Mavanthoor, and V. Chinta, "Analysis of a fixed-guided compliant beam with an inflection point using the pseudo-rigid-body model concept," J. Mech. Rob. **7**, 031007-1–031007-10 (2015).
[28]P. F. Byrd and M. D. Friedman, *Handbook of Elliptic Integrals for Engineers and Physicists* (Springer, 2013), Vol. 67.
[29]S. A. Al-Saleh and R. Z. Al-Zaid, "Effects of drying conditions, admixtures and specimen size on shrinkage strains," Cem. Concr. Res **36**, 1985–1991 (2006).